

Using Deep Learning to Identify Initial Error Sensitivity of ENSO Forecasts

Kinya Toride,^{a,b} Matthew Newman,^a Andrew Hoell,^a Antonietta Capotondi,^{a,b} Jakob Schlör,^c

Dillon Amaya,^a

^a *Physical Sciences Laboratory, National Oceanic and Atmospheric Administration, Boulder, Colorado*

^b *Cooperative Institute for Research in Environmental Sciences, University of Colorado Boulder, Boulder, Colorado*

^c *Machine Learning in Climate Science, University of Tübingen, Tübingen, Germany*

Corresponding author: Kinya Toride, kinya.toride@noaa.gov

ABSTRACT

We introduce a hybrid method that integrates deep learning with model-analog forecasting, a straightforward yet effective approach that generates forecasts from similar initial climate states in a repository of model simulations. This hybrid framework employs a convolutional neural network to estimate state-dependent weights to identify analog states. The advantage of our method lies in its physical interpretability, offering insights into initial-error-sensitive regions through estimated weights and the ability to trace the physically-based temporal evolution of the system through analog forecasting. We evaluate our approach using the Community Earth System Model Version 2 Large Ensemble to forecast the El Niño–Southern Oscillation (ENSO) on a seasonal-to-annual time scale. Results show a 10% improvement in forecasting sea surface temperature anomalies over the equatorial Pacific at 9–12 months leads compared to the traditional model-analog technique. Furthermore, our hybrid model demonstrates improvements in boreal winter and spring initialization when evaluated against a reanalysis dataset. Our deep learning-based approach reveals state-dependent sensitivity linked to various seasonally varying physical processes, including the Pacific Meridional Modes, equatorial recharge oscillator, and stochastic wind forcing. Notably, disparities emerge in the sensitivity associated with El Niño and La Niña events. We find that sea surface temperature over the tropical Pacific plays a more crucial role in El Niño forecasting, while zonal wind stress over the same region exhibits greater significance in La Niña prediction. This approach has broad implications for forecasting diverse climate phenomena, including regional temperature and precipitation, which are challenging for the traditional model-analog forecasting method.

SIGNIFICANCE STATEMENT

The purpose of this study is to demonstrate a skillful and interpretable approach for forecasting the El Niño–Southern Oscillation by combining deep learning and a simple analog forecasting method. A convolutional neural network is used to find important areas for picking analog members. This is important because it is challenging to explain the decision-making processes of recent deep-learning approaches. The developed approach can be applied to various climate predictions.

1. Introduction

The prediction of climate variability over seasonal to interannual time scales greatly depends on the quality of El Niño–Southern Oscillation (ENSO) forecasts. The magnitude and pattern of tropical sea surface temperature (SST) anomalies associated with ENSO influence global climate through atmospheric teleconnections primarily driven by the Walker and Hadley circulations and stationary Rossby wave trains (Alexander et al. 2002; Hoell and Funk 2013; Capotondi et al. 2015; Taschetto et al. 2020). Despite its importance, state-of-the-art atmosphere-ocean coupled models do not exhibit a substantial improvement over simpler linear models in predicting ENSO (Newman and Sardeshmukh 2017; Shin et al. 2021; Risbey et al. 2021).

With recent progress in deep learning, several studies have applied various neural networks to ENSO prediction (Ham et al. 2019; Petersik and Dijkstra 2020; Cachay et al. 2021; Chen et al. 2021; Ham et al. 2021; Zhou and Zhang 2023). Considering the data-intensive nature of deep learning, long-term climate simulations from multiple models are often leveraged to capture nonlinear dynamics of ENSO and mitigate model-specific biases. While these data-driven models exhibit promising performance, interpreting their decision-making processes poses a challenge due to the large amount of hidden parameters. The interpretability of prediction models is crucial since models with better prediction skill can enhance scientific understanding of physical processes, which can, in turn, improve prediction skill. Explainable artificial intelligence (XAI) is frequently used to elucidate neural network models in a post-hoc manner (e.g., Shin et al. 2022). However, different XAI techniques may yield different explanations (Mamalakis et al. 2022), and it remains challenging to explain complex models despite their superior accuracy in general.

Analog forecasting is a simpler method which makes predictions based on similar states that occurred in the past, assuming they follow the attractor of the dynamical system (Lorenz 1969a). While the sample size of historical records is too small to find good analogs for most climate-scale applications (Van den Dool 1989), simulated climate data allow for drawing “model-analogs” from thousands of years of data. Because analog forecasting circumvents issues with initialization shock (Mulholland et al. 2015), this method provides comparable skill to that of coupled atmosphere-ocean models in forecasting seasonal tropical SST (Ding et al. 2018, 2019).

However, tiny disturbances in initial states can grow into significant differences due to the unpredictable nature of the climate system (Lorenz 1963, 1969b). Fig. 1b illustrates this issue where some analogs can evolve to the opposite phase of ENSO in 12 months. The sensitivity to initial conditions varies by location, with certain regions being more prone to initial errors while others are relatively insensitive (Errico 1997; Barsugli and Sardeshmukh 2002). This suggests that assigning higher weights to initial condition-sensitive regions when finding analogs may minimize error growth over the duration of a given forecast.

In this study, we introduce a deep learning method to predict state-dependent weights for selecting model-analogs. The combination of analog forecasting and machine learning has been investigated by several studies. Chattopadhyay et al. (2020) clustered surface temperature patterns into five groups and used a capsule neural network to predict the cluster indices based on states 1–5 days prior. Rader and Barnes (2023) developed a neural network with trainable weights for analog forecasting, but their weights are state-independent and struggle to predict extreme events.

Here, we construct a convolutional neural network to predict weights given an initial condition. Regions with higher weights are considered sensitive to initial errors, and we aim to find analogs that closely match over these regions. Fig. 1c illustrates that analogs selected using predicted weights (hereafter referred to as “optimized model-analogs”) exhibit smaller error growth compared to the original analogs. Our method offers two key advantages in terms of interpretability. First, the estimated weights show regions sensitive to initial conditions where error growth is significant. These weights are directly used for analog forecasting and thus objectively evaluated by forecast skill, unlike the post-hoc explanations provided by XAI. Second, once analogs are identified using weights, we can trace the physically-based evolution of all fields available in the model simulation for any lead time. This is unattainable with a standalone neural network unless it is trained for all variables.

Our approach improves forecast skill of equatorial Pacific SST in both perfect-model and real-world experiments. While many machine learning-driven studies typically focus on predicting simple Niño indices (Ham et al. 2019; Petersik and Dijkstra 2020; Cachay et al. 2021; Chen et al. 2021; Ham et al. 2021; Shin et al. 2022), we aim to improve the prediction of the spatial pattern of equatorial Pacific SST given the considerable diversity of individual ENSO events (Capotondi et al. 2015). Additionally, we explore the connection between the predicted weights and various physical processes associated with ENSO dynamics, including

the asymmetry in initial-error-sensitivity for El Niño and La Niña. We describe our data and methods in Section 2, then evaluate forecast skill in both perfect-model and real-world experiments in Section 3. In Section 4, we investigate initial-error sensitivity through estimated weights. The selection and effects of network size are discussed in Section 5. Finally, Section 6 provides a summary of our results.

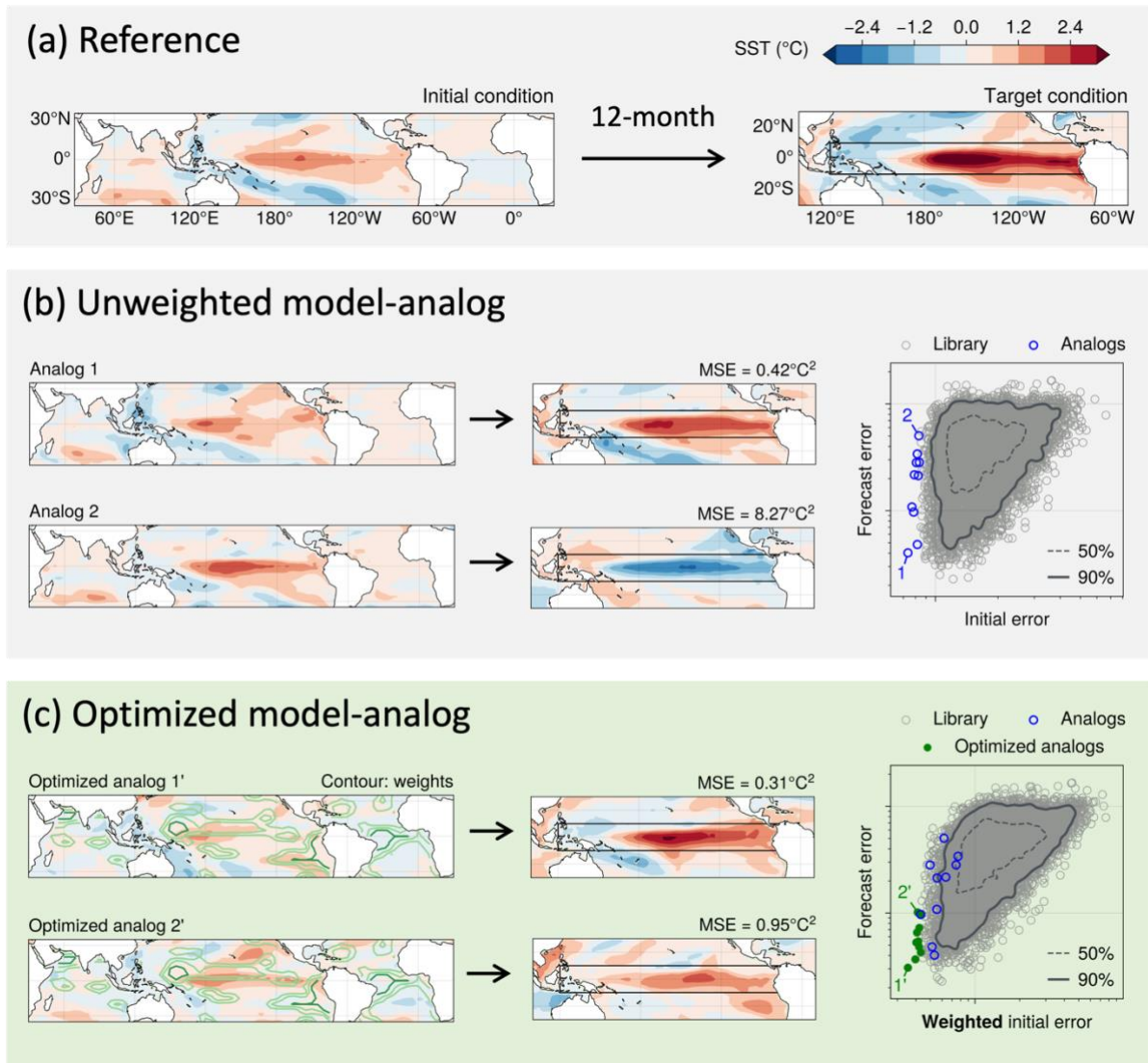


Fig. 1. Schematic method overview of the current study. (a) Reference initial condition for analog selection and target condition 12 months after. The black box in the target condition represents the equatorial Pacific, which is the focus area in this study. (b) Unweighted model-analogs and corresponding forecasts for the best and worst analogs. The mean square errors (MSEs) of the forecasts are shown in each panel. The scatter plot shows initial errors and forecast errors for all samples in the library, along with smoothed probability density curves. Blue circles show 10 analogs with the smallest initial errors. (c)

As in (b), but for the optimized model-analogs which exhibit smaller error growth compared to the original analogs. This method uses deep learning to derive optimized weights for analog selection, displayed by contour lines. The scatter plot uses weighted initial errors on the x-axis. Green circles represent 10 optimized analogs.

2. Methods

a. Data

We first evaluate the hybrid deep learning and model-analog approach within a perfect-model framework. In this framework, the forecast model is assumed to be perfect, with the same model generating training, validation, and test datasets. We use an ensemble of historical simulations from the Community Earth System Model Version 2 Large Ensemble (CESM2-LE; Rodgers et al. 2021). The CESM2-LE historical simulation consists of 100 ensemble members during 1850–2014, resulting in 16,500 years of data. We use monthly mean sea surface temperature (SST), sea surface height (SSH), and zonal wind stress (TAUX) data. These data are interpolated to two different resolutions, $2^\circ \times 2^\circ$ and $5^\circ \times 5^\circ$. The coarser resolution data are used to train the neural network model and to select analogs, while the finer resolution data are used as forecasts after finding analogs. Detrended anomalies are determined by removing the ensemble mean temporally smoothed with a 30-year running mean. Throughout this study, we exclusively use anomalies. We partition the dataset into training (1865–1958; 9400 years, 70%), validation (1959–1985; 2700 years, 20%), and test (1986–1998; 1300 years, 10%) subsets. The training dataset is also used as the library to select model-analogs.

To test the trained model with observed estimates, we use the Ocean Reanalysis System 5 (ORAS5; Zuo et al. 2019) interpolated to the fine and coarse resolution grids. This evaluation uses a fair-sliding anomaly approach that refrains from using future data not available at the time of the forecast (Risbey et al. 2021). Specifically, anomalies are determined by removing the mean and linear trend during the prior 30 years up to the year of the current forecast. Note that our model is not fine-tuned to the reanalysis data.

b. Architecture of the optimized model-analog approach

We leverage a deep learning method to predict weights based on a specified initial condition. To reduce computational cost, we use the coarse resolution data over 50°S – 50°N

(13 latitudes \times 72 longitudes \times 3 variables) as our input. The architecture of the optimized model-analog approach is depicted in Fig. 2. Our chosen model is the U-Net (Ronneberger et al. 2015), a fully convolutional network consisting of a symmetrically designed downsampling encoder followed by an upsampling decoder. While we experimented with variations such as U-Net with residual blocks (He et al. 2015) and with attention gates (Oktay et al. 2018), the differences were minimal.

The encoder in our architecture consists of stacked blocks, each including two convolutional layers and a max pooling operation, halving the spatial resolution while doubling the channel size (i.e., last dimension). Mirroring the encoder, the decoder includes similar stacked blocks where each incorporates a transposed convolutional layer followed by two convolutional layers. This setup reverses the encoder's blocks by doubling the spatial resolution and reducing the channel size by half. Additionally, we use skip connections, which concatenate the features from the downsampling encoder into the decoder at the corresponding level. A final 1×1 convolution aligns the output channel size with the number of input variables.

Two hyperparameters, namely depth and initial channel size, greatly influence the network size. Here, depth corresponds to the number of blocks in the encoder, set as 4 in this study. The initial channel size, set at 64 in our study, is the output channel size of the first encoder block. Either increasing the depth by one or doubling the initial channel size quadruples U-Net parameters. The sensitivity of the obtained results to the network size is discussed in Section 5.

The U-Net predicts weights that are used to determine weighted initial distances from the input initial condition for every sample within the library. The library comprises all states from the training dataset of the corresponding month. The weighted initial distance (d_0) is defined as the sum of weighted mean square errors (MSE_w) of standardized SST, SSH, and TAUX anomalies over 50°S – 50°N .

$$d_0 = MSE_w(\text{SST}) + MSE_w(\text{SSH}) + MSE_w(\text{TAUX}) \quad (1)$$

where MSE_w of standardized anomalies is defined as:

$$MSE_w = \frac{\sum_i w_i \cos \phi_i \left(\frac{x_i}{\sigma_X} - \frac{y_i}{\sigma_Y} \right)^2}{\sum_i w_i \cos \phi_i} \quad (2)$$

Here, i represents a spatial degree of freedom, w represents the weight predicted by U-Net, ϕ denotes latitude, $\cos \phi$ accounts for the grid area weight, x represents the input initial state, and y represents each state in the library. Additionally, σ_x and σ_y represent the square root of domain-averaged variance over the input domain, used for standardization purposes.

The most intuitive training method might be selecting analogs with the smallest weighted initial distances and defining a loss function based on analog forecast errors. However, this approach involves the complex time evolution of the climate model, with unknown analytical derivatives. Thus, we opt for a more efficient strategy to update model parameters.

Initially, the weighted initial distances are sorted, and samples with the lowest weighted initial distances are selected, specifically the top 2% of samples. We focus on these subsamples so that the network is not affected by samples that significantly deviate in initial conditions. As the network is updated and predicts different weights, a different set of subsamples is selected. Note that the sensitivity to the number of retained samples is relatively low. The loss function is defined as the mean-square-error (MSE) between the normalized weighted initial distances (d_0) and forecast errors (d_τ) of the chosen subsamples, where the forecast error is defined as the MSE of SST over the equatorial Pacific (10°S–10°N, 120°E–70°W; black box in Fig. 1) at a certain lead time (τ). The loss function L_i for the given initial condition (sample index i) can be expressed as:

$$L_i = \frac{1}{n_{sub}} \sum_j^{n_{sub}} \left(\frac{d_{0,j}}{\max_{j \in n} d_{0,j}} - \frac{d_{\tau,j}}{\max_{j \in n} d_{\tau,j}} \right)^2 \quad (3)$$

where j represents the index of samples, n_{sub} represents the number of subsamples, and n represents the number of samples in the library. The weighted initial distances and forecast errors are scaled by the respective maximums. Minimizing the loss guides the U-Net to estimate weights that prioritize samples with smaller forecast errors to have smaller weighted initial distances. Essentially, the objective is to maintain consistency in initial and forecast errors across the subsamples. This iterative process is executed for each sample in the training dataset, constituting one epoch.

Although the U-Net can be trained for various lead times (τ), it results in identifying different analogs for different lead times. This compromises one of the advantages of analog forecasting—the ability to track the time evolution of the system. To address this, we train the U-Net using forecast errors (d_τ) defined by the mean of MSEs across 3, 6, 9, and 12-

month lead times over the equatorial Pacific. This approach yields comparable results to training for specific lead times (6, 9, or 12 months), as detailed in Appendix B.

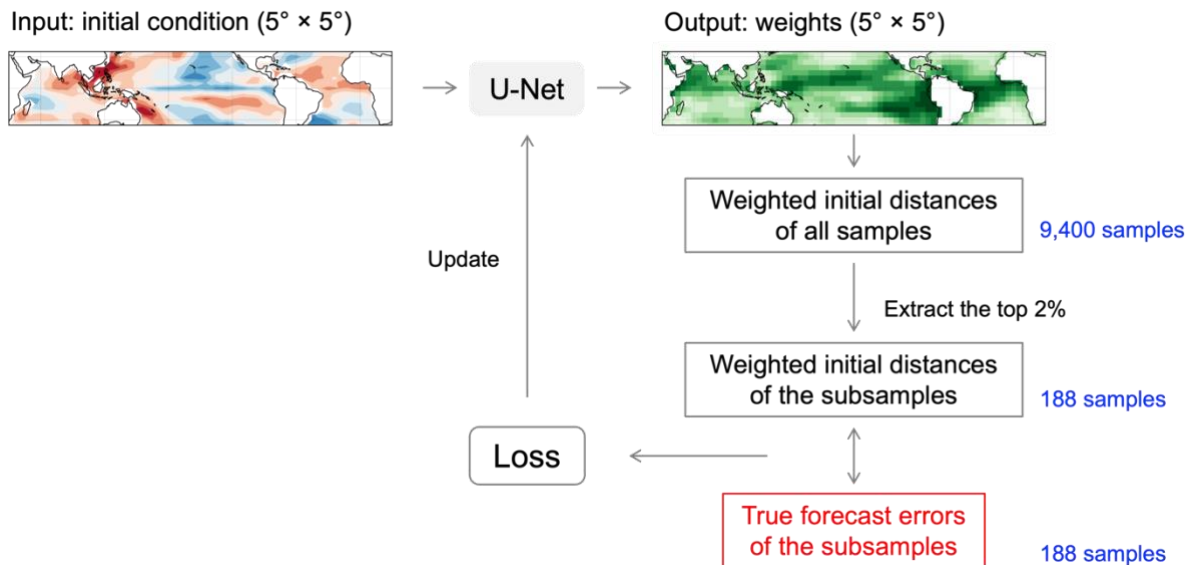


Fig. 2. Architecture of the optimized model-analog approach.

During each epoch, we monitor ensemble-mean forecast error at 12 months lead. Here, we choose 30 analog members (see Appendix A for details). The maximum number of epochs is capped at 60, and we use early stopping to prevent overfitting, i.e. training is stopped when the ensemble-mean forecast error in the validation dataset ceases to decrease. The Adam optimizer (Kingma and Ba 2017) is used to update network parameters. We train the model 10 times to account for the random initialization of U-Net parameters. Since analog selection is performed within the library of the corresponding month, we train a separate U-Net for each month. The source code is available at GitHub (<https://github.com/kinyatoride/DLMA>).

c. Hyperparameter tuning

Key hyperparameters considered in this study are the initial channel size, depth, learning rate, and subsample size. In the initial phase of hyperparameter tuning, we focus on January initialization with a lead time of 12 months. This choice is motivated by the largest ENSO variability observed during this month in the model. All hyperparameters are optimized based on ensemble-mean forecast error in the validation dataset with a 12-month lead time.

Upon completing the tuning process, the same set of hyperparameters is adopted for other initialization months, with the exception of the learning rate. Due to the significant impact of the learning rate, we fine-tune this parameter independently for each month.

d. Unweighted model-analog and neural network-only approach

We compare our hybrid approach against both the plain model-analog and an equivalent neural network-only approach.

The plain model-analog approach draws analogs based on unweighted distance (Ding et al. 2018, 2019; Lou et al. 2023). Here, distance is defined as the sum of MSEs of standardized SST and SSH over 30°S–30°N. MSE is similar to the formulation in Eq. (2) but with a constant weight ($w = 1$). The number of analog members is set to 30. In contrast to the hybrid method, distances are calculated using the 2° data since no training is required. TAUX and extratropical regions are omitted in this approach, as their inclusion has been found to degrade skill. More discussion can be found in Appendix A.

To address the question of whether combining deep learning and analog forecasting might downgrade the deep learning capabilities, we compare the results with a neural network-only method using a similar architecture. We use the same U-Net architecture except for the final layer. The final 1×1 convolution is adjusted to generate fine-resolution SST fields over the equatorial Pacific. Consequently, this approach takes 5° SST, SSH, and TAUX fields over 50°S–50°N as input and predicts 2° SST over the equatorial Pacific. Given the discrepancy in dimension sizes between inputs and outputs, we apply additional padding and cropping of the data. The number of trainable parameters in this modified U-Net differs from the original by less than 0.01%. While the initial channel size and depth are the same as the original, we tune the learning rate separately for this model. Note that this model is only evaluated for January initialization.

e. Evaluation metrics

We use root-mean-square error (RMSE) and uncentered anomaly correlation square (AC^2) to assess the performance of ensemble-mean forecasts. AC^2 is specifically defined as $AC^2 = (\max(AC, 0))^2$, ensuring that negative correlations are treated as zero.

To test the statistical significance of the improvements achieved through the optimized analog approach over the unweighted approach, we conduct a one-sided permutation test

(resampling without replacement) using the time-series of forecasts. The null hypothesis is that the true improvement is zero, which is rejected at the significance level of 5%. The null distribution is constructed through 10,000 permutations. When multiple hypotheses are simultaneously tested, as for a map of gridded data, Wilks (2016) recommends adjusting the threshold p-value for the number of false discoveries. We use the Benjamini and Hochberg step-up procedure (Benjamini and Hochberg 1995) with a 5% false discovery rate.

To evaluate the probabilistic skill, we use the continuous ranked probability score (CRPS), which corresponds to the integral of the Brier score over all possible threshold values. CRPS can be decomposed into three components: reliability, resolution, and uncertainty (Hersbach 2000). Reliability reflects the flatness of the rank histogram and resolution is linked to the ensemble spread.

3. Forecast verification

a. January initialization

Fig. 3 shows perfect model skill using both unweighted and optimized model-analog methods for January initialization, with the test dataset spanning 1,300 years. The application of deep learning significantly enhances analog selection when forecasting SST patterns over the equatorial Pacific. RMSE is reduced by 10% for a lead time of 9–12 months (Fig. 3a), and AC^2 of 0.4 is extended by more than 2.5 months (Fig. 3b). These improvements remain robust and are minimally affected by random initialization of the training, as indicated by the orange shade. However, for shorter lead times (i.e., 1–2 months lead), the optimized approach exhibits worse forecast errors, suggesting that the neural network assigns more weights to regions beyond the target area to select analogs with better forecasts in longer leads. Consequently, the unweighted approach, which allocates relatively more weights over the equatorial Pacific, results in lower forecast errors for shorter leads.

Figs. 3c–d illustrate the spatial distribution of RMSE reduction and the increase in AC^2 achieved by the optimized approach. Skill is consistently improved east of the Maritime Continent, with particular improvement around the Niño 3.4 region in the central equatorial Pacific. However, over the Maritime Continent, neither RMSE nor AC^2 exhibits significant improvements, primarily due to the small SST variability in the region and the use of MSE in the loss function. The hybrid approach enhances skill in the central equatorial Pacific, where unweighted model-analogs exhibit the highest skill (Ding et al. 2018).

Although the optimized model-analog approach significantly improves analog forecasting, a question arises regarding whether a standalone neural network may produce better forecasts. Figs. 3a–b display the forecast skill of the equivalent neural network-only method. It is important to note that this method can only generate forecasts at a single lead. Thus, we separately train the model for 3, 6, 9, and 12 months leads. While the neural network-only method exhibits better skill at 3 and 6 months leads, it demonstrates similar skill at 9 and 12 months leads. With respect to AC^2 , the optimized model-analog approach shows better accuracy at these leads, where this approach exhibits largest improvements (see Appendix B). These results demonstrate that the combination of neural network and model-analog not only provides an advantage for tracking full-state evolution, but also yields comparable forecast skill compared to a neural network-only approach with a similar architecture and training efforts.

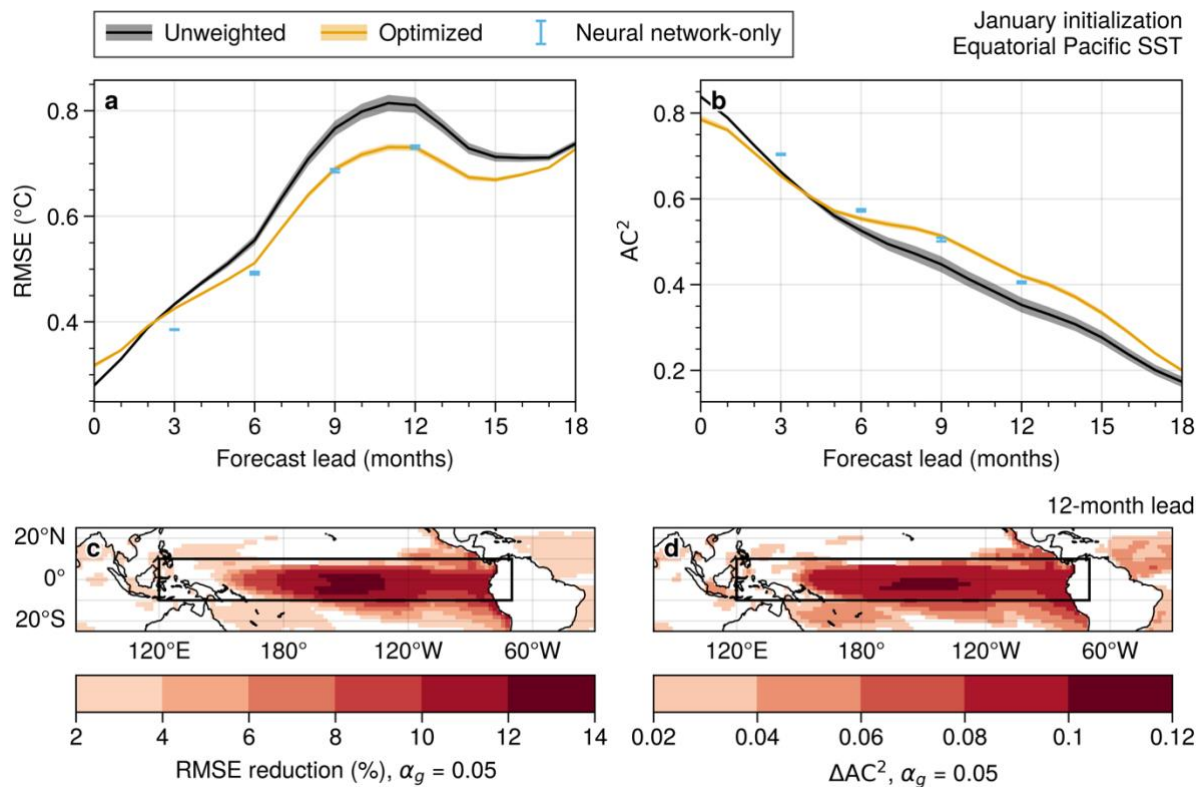


Fig. 3. Forecast skill comparison among the unweighted model-analog, optimized model-analog, and neural network-only approaches for January initialization using the test dataset. (a) Root-mean-square error (RMSE) of equatorial Pacific SST as a function of forecast lead. The black shading represents the 95% confidence interval estimated through the permutation test between unweighted and optimized results. The orange shading and blue error bars show

the spread due to random initialization of network parameters. (b) Similar to (a), but for square anomaly correlation (AC^2) averaged over the equatorial Pacific. (c) RMSE reduction (%) of 12-month lead SST by the optimized approach compared to the unweighted approach. (d) Similar to (c), but for the increase in AC^2 . In (c) and (d), color shading indicates statistically significant improvements at the 5% level with the 5% false discovery rate.

b. All-month initialization

Having tuned the hyperparameters for January initialization, we extend the application of the optimized model-analog approach to other initialization months. Fig. 4 shows the seasonal variation of perfect-model AC^2 averaged over the equatorial Pacific. In general, optimized model-analog yields consistent impacts on analog forecasting across all initialization months. While the forecast skill tends to be lower for shorter leads as the neural network places more weights outside the target region, substantial improvements are observed for longer leads ranging from 6 to 18 months. These improvements are particularly notable for initialization during boreal winter and spring (Nov–Apr), with verification during boreal fall and winter (Sep–Mar).

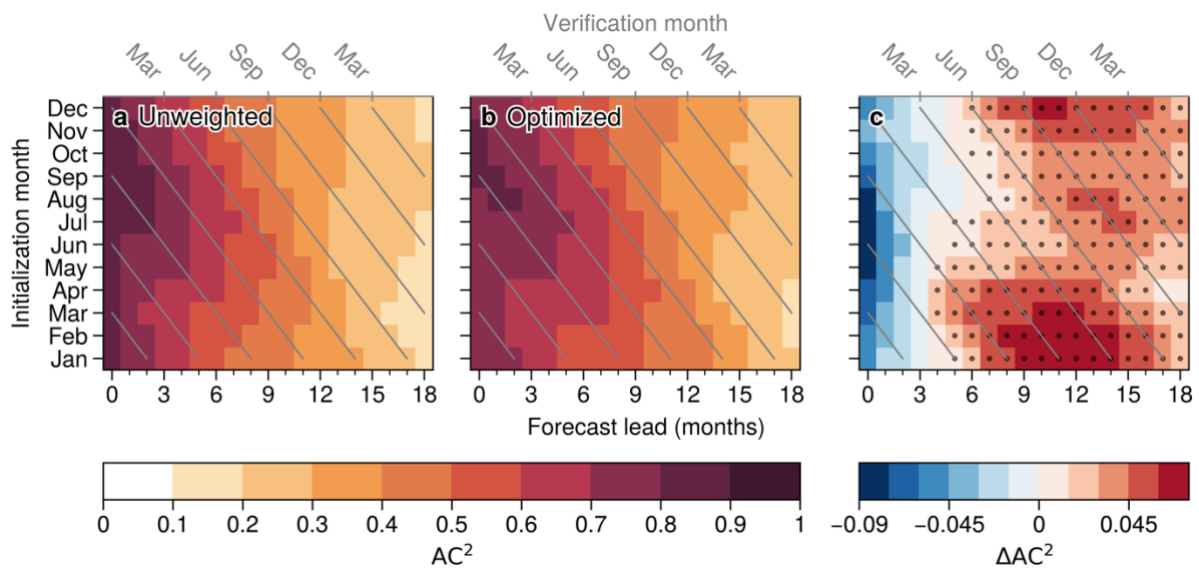


Fig. 4. The seasonality of square anomaly correlation (AC^2) of SST averaged over the equatorial Pacific as a function of forecast lead. (a) The unweighted model-analog, (b) optimized model-analog, and (c) the difference between the two approaches. Stippling in (c) indicates statistically significant improvements. The verification month is indicated by the gray diagonal lines.

In Fig. 5, we present the all-month probabilistic forecast skill using 30 analog members. CRPS exhibits similar behavior to the ensemble-mean skill, showing lower skill for shorter leads and enhanced skill for longer leads. CRPS of 0.4°C is extended for more than 1 month on the all-month average. The improvements in CRPS are attributed to improvements in resolution or ensemble spreads (Fig. 5c). This is logical given that the loss function is designed to penalize samples deviating significantly at forecast leads, resulting in narrower ensemble spreads. However, smaller ensemble spreads can deteriorate the reliability component, associated with the flatness of the rank histogram (Fig. 5b). The rank histogram is the frequency of the rank of the verification relative to sorted ensemble members. In the absence of ensemble variability, the rank histogram tends to exhibit a U-shaped distribution (Hamill 2001). Since ensemble reliability was not explicitly considered in the loss function, this stands as one of the caveats in this study.

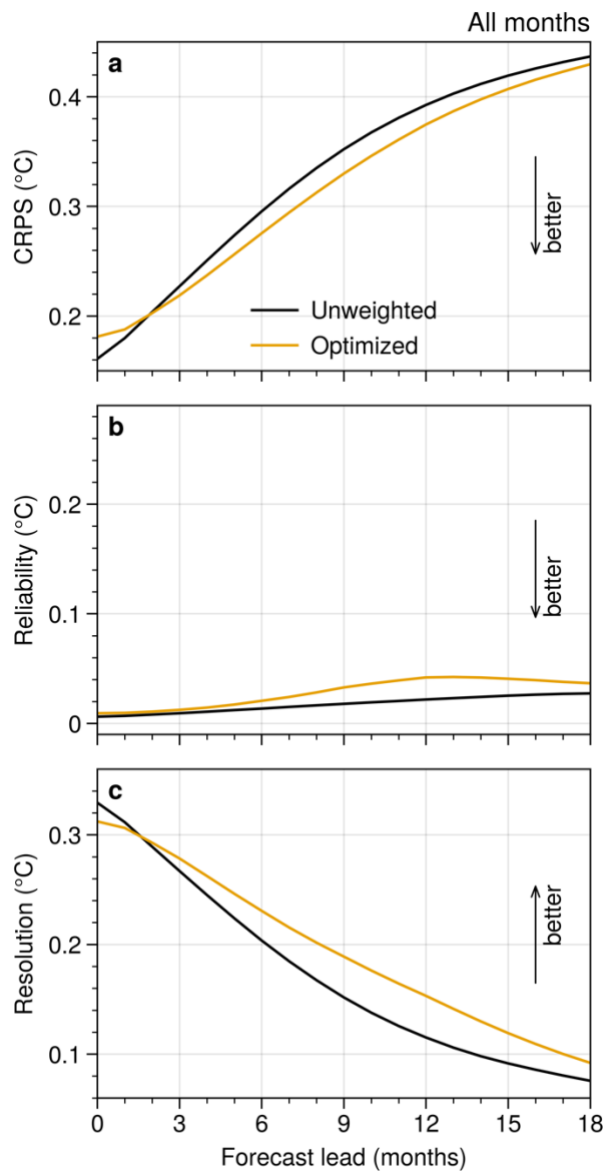


Fig. 5. (a) Seasonally-averaged continuous ranked probability score (CRPS) of SST over the equatorial Pacific as a function of forecast lead by the unweighted and optimized model-analog methods. Similar to (a), but for (b) reliability and (c) resolution components of the CRPS.

Once analogs are identified, forecasting can be extended to any field available in the climate simulation. This is a distinct advantage in analog forecasting not achievable solely with neural networks, where predictors and predictands must be carefully chosen based on specific phenomena targeted by the model and the available computational resources. Fig. 6 shows the improvements in 12-month precipitation forecasting using the optimized model-

analog. Precipitation forecasting is particularly improved in DJF (Fig. 6a), with significant improvements extending beyond the target region including the central subtropical Pacific, Maritime Continent, southwest Pacific east of Australia, southeastern US, northeastern Brazil, and north of Madagascar, potentially linked to ENSO teleconnections. Similarly, forecast skill in MAM is improved both within and outside the target region, albeit with smaller magnitudes (Fig. 6b). While precipitation forecast skill in JJA and SON also displays significant improvements, the impact is primarily confined within the target region (Figs. 6c,d). It is essential to highlight that, while not always statistically significant, positive impacts on precipitation forecasting are observed in most regions across all seasons (not shown). This suggests that improving ENSO forecasts contributes positively to global precipitation forecasting.

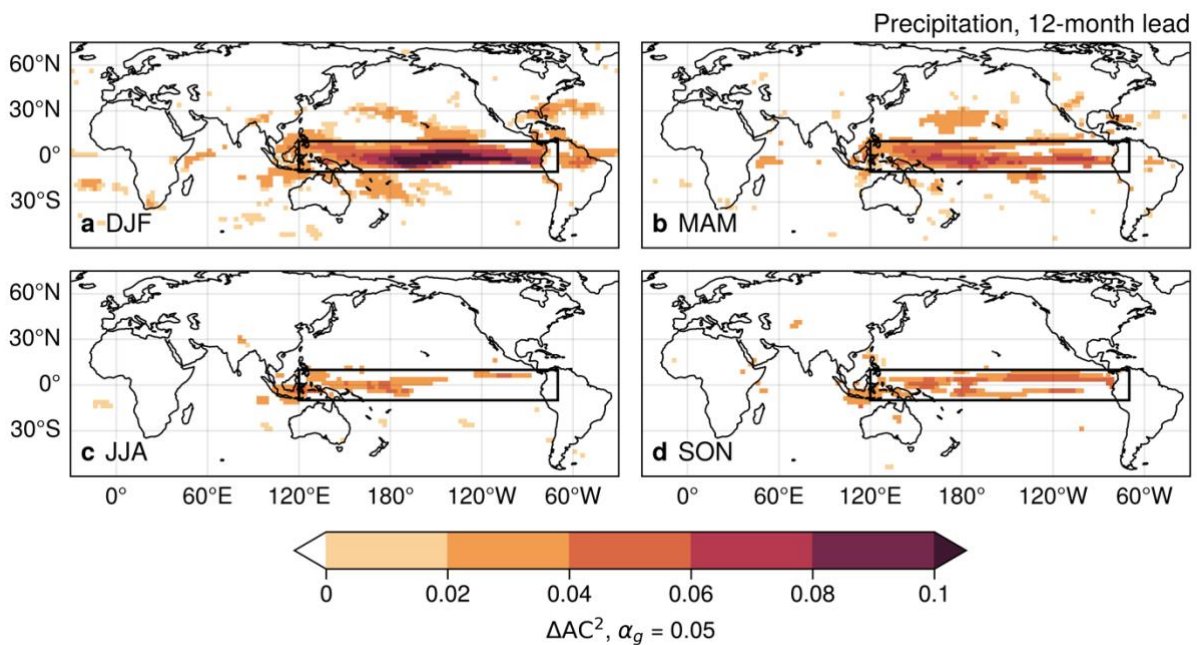


Fig. 6. Increase in square anomaly correlation (AC²) of 12-month lead precipitation by the optimized approach compared to the unweighted approach. The forecasts are initialized and verified for (a) DJF, (b) MAM, (c) JJA and (d) SON. Color shading indicates statistically significant improvements at the 5% level with the 5% false discovery rate.

c. Hindcast

We apply the developed optimized model-analog approach to a reanalysis dataset, using the same network with a limited training epoch of 10 to prevent overfitting to the CESM2 climate. No transfer learning is employed in this study. Fig. 7 shows the seasonal variation of hindcast skill during 1987–2020. The unweighted model-analog shows lower skill than the

perfect-model skill with a spring predictability barrier where skill sharply declines around March (Fig. 7a). The impact of the optimized approach varies across initialization months (Fig. 7c). Although positive effects are observed in many initialization months, forecasts initialized in Aug–Oct display a decrease in skill. Statistically significant improvements are observed in boreal fall forecasts initialized in May and June, as well as in year 2 spring forecasts initialized in boreal winter.

Despite some positive improvements, several factors contribute to the degraded results relative to the perfect-model results. Climate models inherently possess systematic errors, such as the excessive westward extension of the SST anomalies associated with ENSO (Bellenger et al. 2014), which is also evident in the CESM2 model (Capotondi et al. 2020). If the neural network learns a model attractor that is significantly different from reality, it can deteriorate skill. A potential solution to mitigate model biases involves employing multiple climate models, as demonstrated in model-analog studies (Ding et al. 2018, 2019; Lou et al. 2023), and machine learning studies (Ham et al. 2019; Zhou and Zhang 2023). Transfer learning may also alleviate biases, although with limitations due to sample size and the effects of climate change. Additional reasons for less significant results include a limited sample size, uncertainty in the fair-sliding anomaly calculation method, and initial conditions uncertainty in the reanalysis dataset.

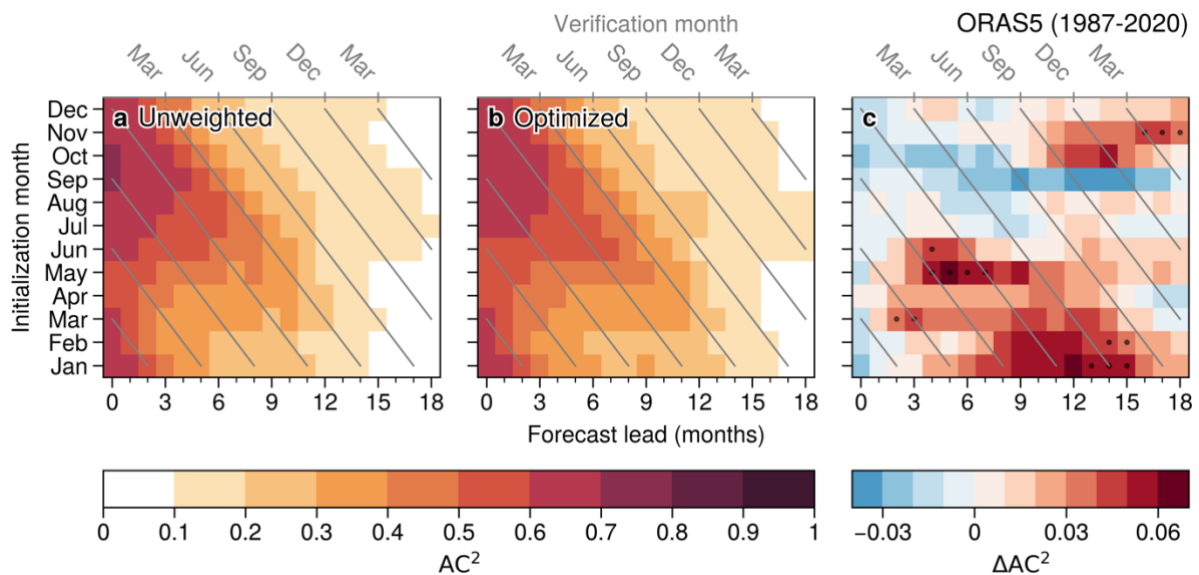


Fig. 7. Similar to Fig. 4, but for hindcast initialized during 1987–2020 using ORAS5.

Fig. 8 illustrates the ENSO conditions under which forecasts are improved for both perfect-model and reanalysis experiments using 12-month forecasts initialized in January. It is evident that forecasts for extreme events are improved in the test dataset for both El Niño and La Niña conditions (Fig. 8a), due to their large influences in the loss function. Conversely, forecasts for ENSO neutral conditions (below 0.5σ) show no discernible impacts on the median. Although the sample size is small, a similar trend is observed in the hindcast (Fig. 8b). With the exception of the La Niña event in 1996, the optimized approach improves forecasts for all extreme events above 1σ . However, issues with model errors are also apparent. In Fig. 8a, extreme events most influenced by the optimized approach exhibit Niño 3.4 values much higher than historically observed values, suggesting that the neural network may be learning information not applicable in the real world. This may also account for the inconsistent impact on weak ENSO forecasts (between 0.5σ and 1σ) in Fig. 8b, as these events correspond to nearly neutral conditions in CESM2.

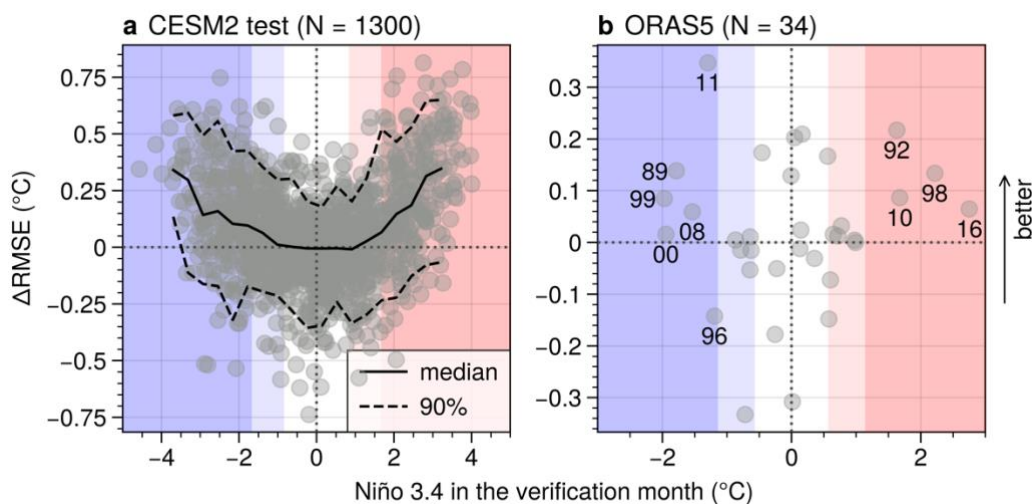


Fig. 8. Scatter plots of the RMSE reduction of SST over the equatorial Pacific and the Niño 3.4 index in the verification month for (a) the CESM2 test dataset and (b) ORAS5. The analysis focuses on 12-month forecasts initialized in January. Lighter pink/blue colors show values above 0.5σ and darker pink/blue colors show values above 1σ of the respective Niño 3.4 index in CESM2 and ORAS5. In (a), the median and 90% lines are estimated by binning samples according to the Niño 3.4 index. In (b), the last two digits of verification years are displayed for extreme events.

4. Interpretable weights

The neural network in the optimized model-analog approach produces interpretable weights that are state-dependent and can be regarded as indicators of sensitivity. Similar to XAI methods, these weights do not provide causal relationships. Instead, they highlight the regions that could most effectively constrain target evolutions through both physical processes and correlated or dependent features. Fig. 9 illustrates the mean weights for four initialization months using the CESM2 test dataset. Recall that these weights improve forecasts at 6–18 months lead (Fig. 4). Generally, the weights are allocated to similar regions year-round. However, depending on the season, the relative magnitudes of weights differ, indicating varying importance of specific processes or regions. Importantly, weights allocated to the target region (equatorial Pacific SST, indicated by the black box) do not dominate the total weights. This explains the reduced forecasting skill over the target area in shorter leads. Furthermore, most of the weights are distributed within the tropics (30°S – 30°N), suggesting that extratropical contribution is small.

The distribution of weights to the three variables varies by season, as shown in Fig. 10. From October to March, the weights are distributed relatively evenly among SST and SSH, with smaller weights attributed to TAUX. April presents a deviation, with SST receiving the largest weights followed by SSH and TAUX. From May to September, the emphasis shifts, with TAUX receiving larger weights compared to SSH. Notably, TAUX receives the largest weights among all variables during June and July.

The spatial distributions of weights reveal connections to various physical processes associated with ENSO. In January (Fig. 9a) and April (Fig. 9d), SST receives weights that extend southwestward from the California coast toward the western equatorial Pacific, as well as over the eastern equatorial Pacific. This pattern closely resembles the characteristics of the North Pacific Meridional Mode (NPMM) (Chiang and Vimont 2004; Amaya 2019), a robust predictor of ENSO conditions (Penland and Sardeshmukh 1995; Larson and Kirtman 2014; Vimont et al. 2014; Capotondi and Sardeshmukh 2015; Capotondi and Ricciardulli 2021). The NPMM typically peaks in boreal spring, aligning with our findings where larger weights are assigned in April to June (Fig. 11a). Additionally, the SST weights in the subtropical southeastern Pacific resemble the pattern of the South Pacific Meridional Mode (SPMM) (Zhang et al. 2014), particularly evident in January (Fig. 9a) and October (Fig. 9j). The air-sea coupling associated with SPMM peaks in boreal winter (You and Furtado 2018), consistent with our findings (Fig. 11b). Regarding the July initialization (Fig. 9g), SST

weights concentrate more over the eastern equatorial Pacific. This reflects the timing of ENSO events in boreal winter and their influences on subsequent seasons, which are the target leads of the July initialization.

SSH weights are consistently focused over the equatorial Pacific throughout the year, unlike SST (Figs. 9b, e, h, and k). Since SSH is dynamically linked to thermocline depth, this pattern likely relates to the recharge and discharge of upper-ocean heat content during the alternation of warm and cold ENSO phases (Jin 1997). In particular, a recharged state is conducive to the development of an El Niño, while a discharged state may likely lead to a La Niña. The equatorial weights can constrain the zonal tilt of the equatorial thermocline concurrent with the peak of ENSO, in addition to the recharge-discharge mode which is an important precursor of ENSO (Meinen and McPhaden 2000). Notably, these weights are particularly amplified in April (Fig. 11c). Equatorial Pacific upper-ocean heat content typically precedes Niño 3.4 SST by a quarter of the ENSO cycle (McPhaden 2003), equating to about 8–10 months in CESM2 (Capotondi et al. 2020). Given that ENSO events tend to peak in boreal winter, the peak of weights in April is consistent with these established temporal dynamics.

Winds play a crucial role in driving ENSO variability. TAUX weights tend to be largest in the western to central tropical Pacific throughout the year (Figs. 9c, f, i, and l), coinciding with the typical occurrence of stochastic wind forcing across the region. This stochastic forcing exhibits a broad spectrum ranging from subseasonal to interannual scales, with the lower frequency component often exerting a greater influence on ENSO evolution (Roulston and Neelin 2000; Capotondi et al. 2018). During boreal summer, the absence of the interannual component of stochastic wind can restrict ENSO growth (Menkes et al. 2014), elucidating the peak magnitude of wind weights observed in June (Fig. 11d).

Although the primary focus lies on the tropical Pacific, allocation of weights to the Atlantic and Indian Ocean indicates the impacts of tropical interbasin interaction (Cai et al. 2019; Wang 2019). Interestingly, larger weights are distributed to SSH compared to SST over the Atlantic Ocean (Fig. 11). While SST is a source of atmospheric teleconnections (Alexander et al. 2002), our result suggests that SSH may serve as a more reliable proxy for Atlantic influences compared to SST, which may be influenced by other processes. SSH reflects changes in thermocline depth which plays an important role in the surface

temperature distribution. In contrast, large SST weights are observed over the Indian Ocean in January and April, near the Indian Ocean Dipole region.

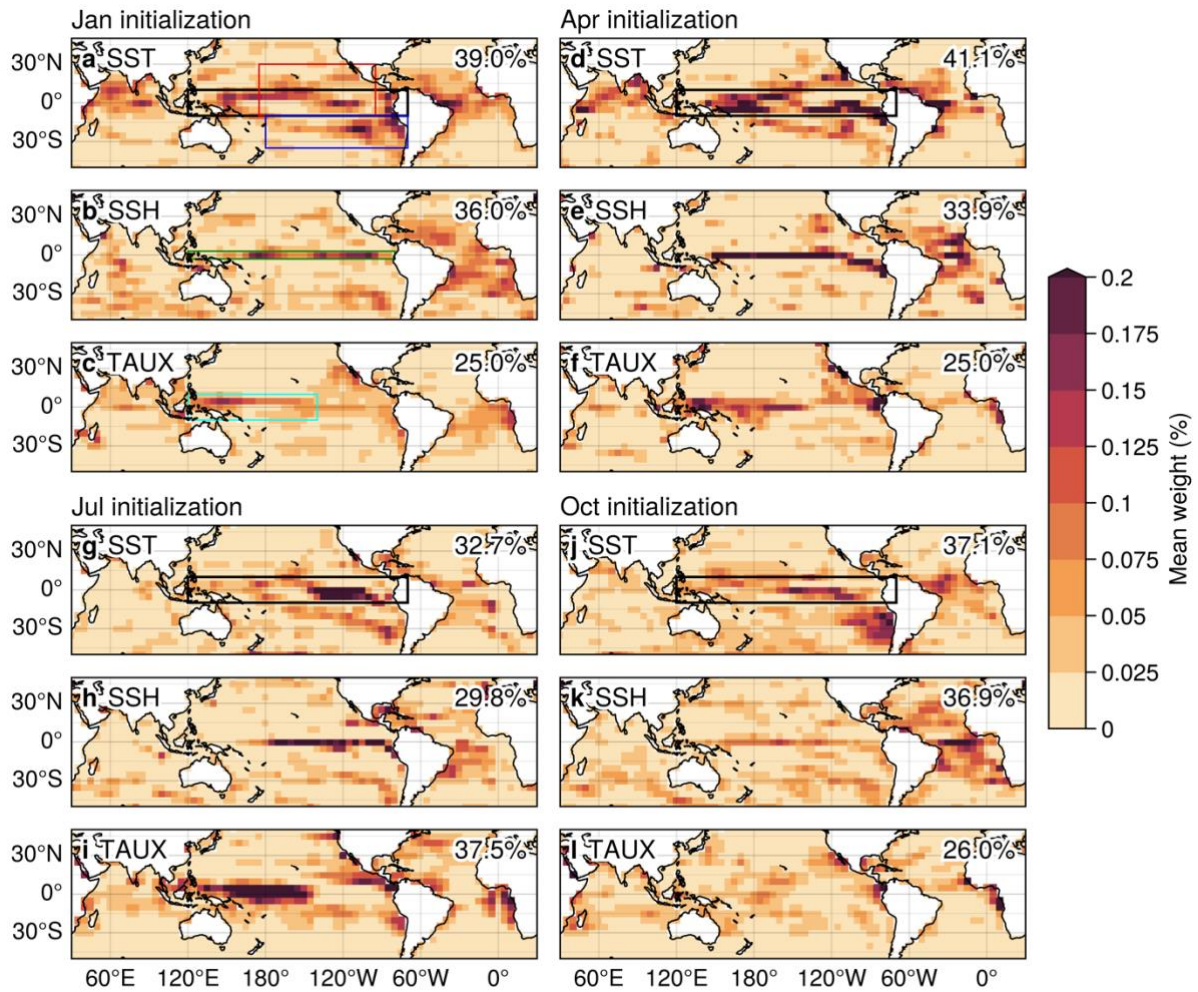


Fig. 9. Mean weights for (a–c) January, (d–f) April, (g–i) July, and (j–l) October initialization in the CESM2 test dataset. These weights improve the selection of analogs for forecasts with lead times of 6–18 months. Weights are unitless and scaled to ensure a sum of 100%. The sum of weights for each variable is displayed within each respective panel. Regions of interest, denoted by red (NPMM SST), blue (SPMM SST), green (equatorial Pacific SSH), and cyan (western to central tropical Pacific TAUX) boxes, are analyzed in Fig. 11.

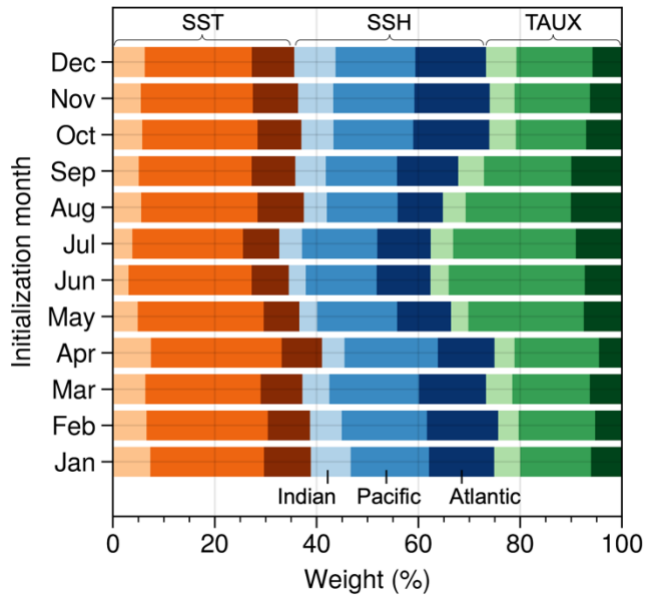


Fig. 10. Seasonal variation of mean weights in the CESM2 test dataset. Red, blue, and green represent the total weights for SST, SSH, and TAUX, respectively. The intensity of light, medium, and dark colors indicates the sum of weights over the Indian, Pacific, and Atlantic Oceans, respectively.

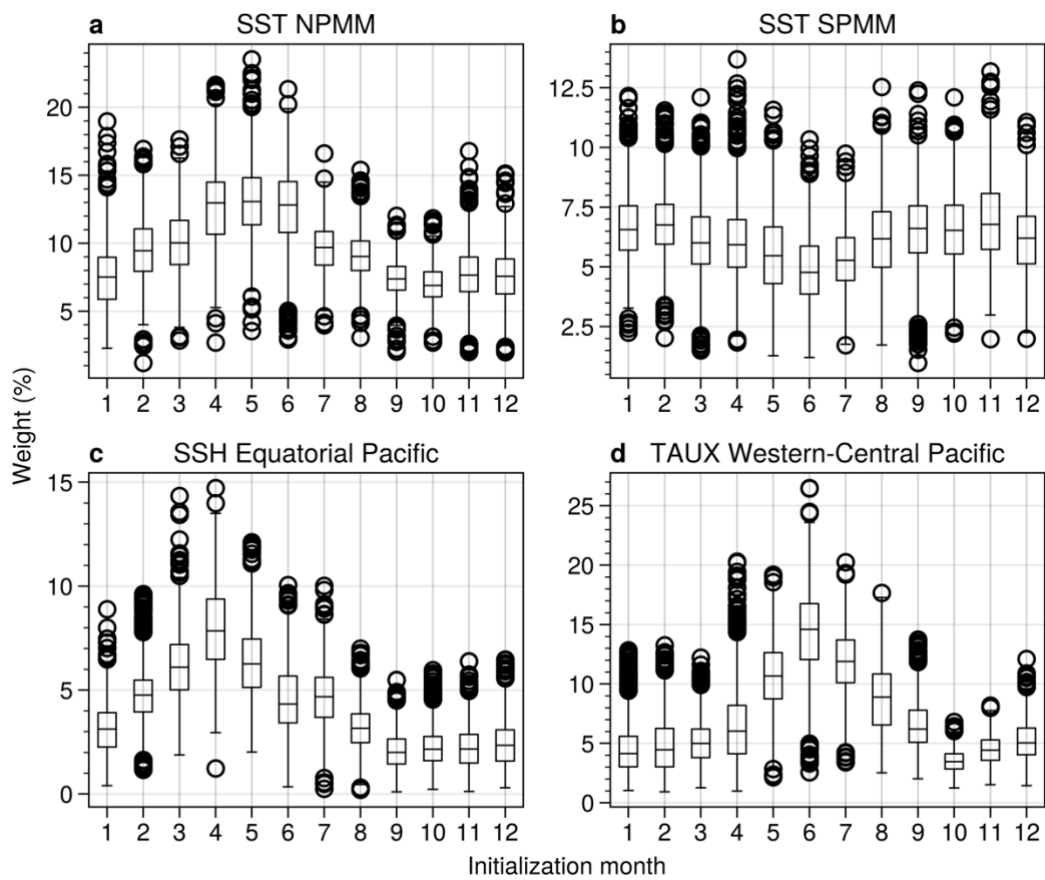


Fig. 11. Seasonal variation of (a) SST weights over the NPMM region (10°S–30°N, 175°E–85°W), (b) SST weights over the SPMM region (35°S–10°S, 180°–70°W), (c) SSH weights over the equatorial Pacific (2.5°S–2.5°N, 120°E–80°W), and (d) TAUX weights over the western to central tropical Pacific (10°S–10°N, 120°E–140°W), as observed in the CESM2 test dataset. Box plots depict the minimum, maximum, median, first and third quantiles, and outliers.

Since weights are state-dependent, we can analyze the asymmetry in sensitivity associated with El Niño and La Niña. Fig. 12 shows the comparison of mean weights for events evolving to El Niño and La Niña 12 months later, initialized in January. Here, El Niño and La Niña events are defined by above and below $\pm 0.5 \sigma$ of the Niño 3.4 index. The spatial distribution of weights generally exhibits similarities to the overall mean (Fig. 9a–c), but differences in magnitude can be observed. Specifically, the SST weights over the Pacific exhibit larger magnitudes for El Niño and weaker magnitudes for La Niña (Fig. 12g). Furthermore, Pacific TAUX weights, particularly along the NPMM region, are larger for La Niña (Fig. 12i).

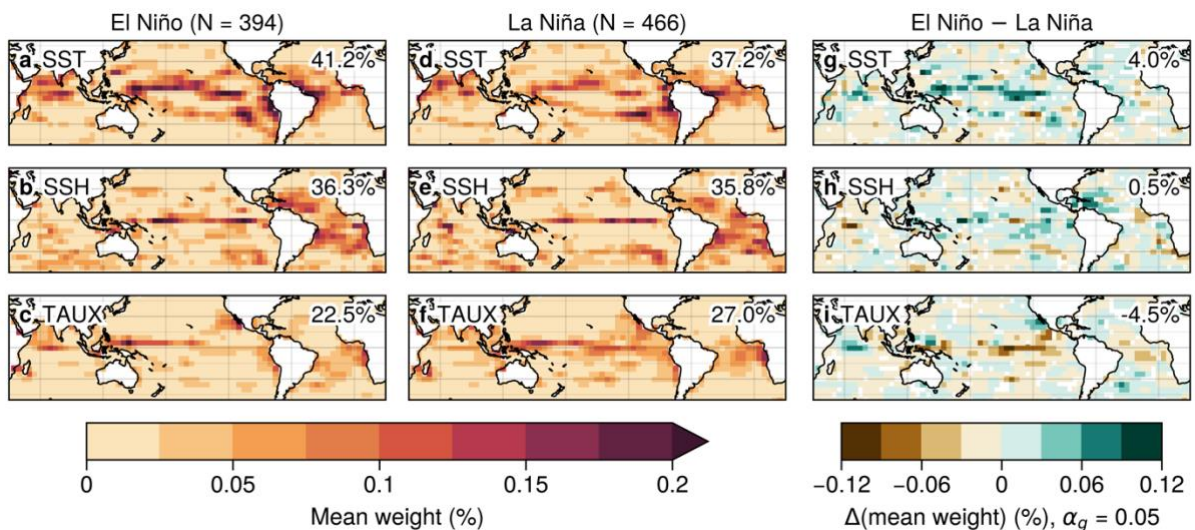


Fig. 12. Mean weights for events that evolve to (a–c) El Niño and (d–f) La Niña conditions in 12 months using January initialization. (g–i) The difference in mean weights between El Niño and La Niña. Color shading indicates statistically significant differences at the 5% level with the 5% false discovery rate.

Given that weights are estimated based on initial conditions, we further subdivide the samples to examine whether the observed differences are dependent on initial conditions. Fig. 13 shows similar differences but specifically for El Niño initial conditions (Figs. 13a–c) and for La Niña initial conditions (Figs. 13d–f). Overall, El Niño initial conditions exhibit similarities and enhanced differences compared to the unconditioned results, while La Niña initial conditions reveal distinct patterns in contrast to the unconditional results. These findings suggest that the identified difference in sensitivity is contingent on initial conditions from which they originate.

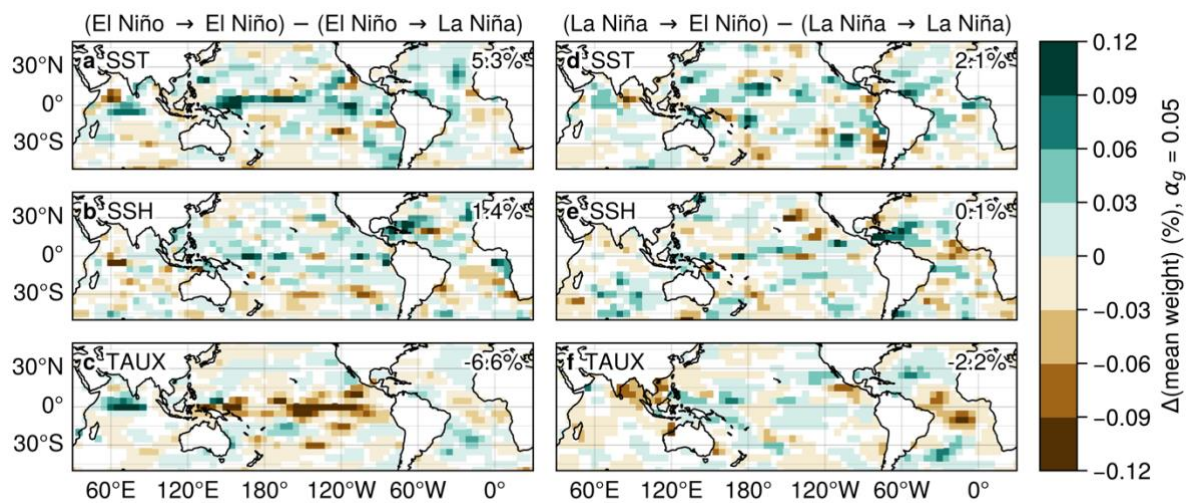


Fig. 13. (a–c) The difference in mean weights between events transitioning from El Niño to El Niño (N=86) and from El Niño to La Niña (N=190). (d–f) The difference in mean weights between events transitioning from La Niña to El Niño (N=104) and from La Niña to La Niña (N=159). Color shading indicates statistically significant differences at the 5% level with the 5% false discovery rate.

5. Network size

The complexity of a model, often indicated by the number of parameters, plays an important role in machine learning studies. Although the trend in the field leans towards more complex models with advanced skill, it is equally important to explore the potential gains achievable with simpler models, especially for those with resource constraints. As described in the Methods section, the network size is controlled by two key hyperparameters: depth and initial channel size. We employ a depth of 4 and an initial channel size of 256 in this study (referred to as 4-256), resulting in 123 millions of trainable parameters. This is determined through hyperparameter tuning and training cost considerations.

Either reducing the depth by 1 or halving the initial channel size decreases the number of parameters by four times. We found that reducing the depth degrades model performance more than reducing the initial channel size. This may be due to the reduction in the receptive field size, which represents the region in the input space influencing an output in a single grid, associated with decreasing depth. Since forecasting ENSO requires capturing large-scale teleconnections as illustrated in the estimated weights (Fig. 9), maintaining a deep network is imperative. Although it is tempting to have a deeper network, the current input size limits the depth to 4.

Therefore, we conduct a sensitivity analysis by varying the initial channel size. Fig. 14a shows the reduction in RMSE on the validation dataset for different network sizes. As the network size increases, the skill improvement follows an asymptotic trend. Statistical tests reveal no significant difference between the 4-256 model and the 4-64 model, which has 16 times fewer parameters. Yet, a significant difference is observed between the 4-512 and 4-64 models (not shown). Hence, one needs to consider the trade-off between computational costs and model performance.

The training duration for the 4-256 model is approximately 30 minutes and 1 hour with a single NVIDIA A100 and A6000 GPU, respectively (Fig. 14b). While the training time decreases with a smaller model, the difference diminishes for models with an initial channel size smaller than 128. This is due to the sorting of samples in the library, as shown in Fig. 2. With smaller networks, sorting time dominates, while larger networks exponentially increase training time. It is essential to note that actual training time and sensitivity to network size may vary depending on the system used.

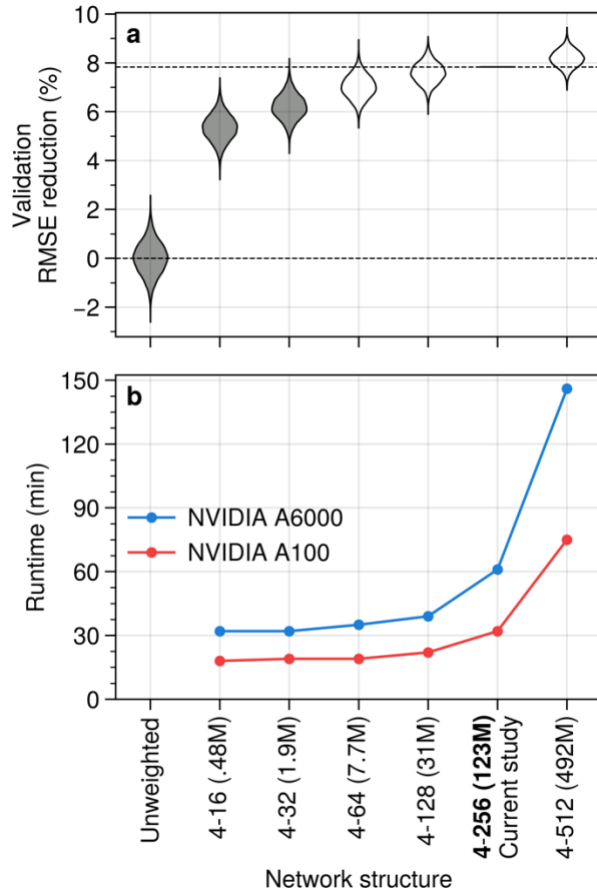


Fig. 14. (a) RMSE reduction (%) of 12-month lead SST over the equatorial Pacific in the validation dataset for different network structures. The network structure is denoted by depth- (initial channel size) with parameter counts in parentheses. Violin plots illustrate the null distribution estimated through permutation with the 4-256 model results. Gray shading indicates values are significantly different at a 5% level. (b) Approximate time taken to train U-Net models for 60 epochs using a single NVIDIA A6000 or A100 GPU in this study.

6. Conclusion

In this study, we demonstrate that deep learning can enhance the potential of analog forecasting. The hybrid optimized model-analog approach can yield comparable forecast skill to a standalone neural network approach, while offering additional benefits associated with analog forecasting. This approach generates interpretable, state-dependent weights that are used to select analog members. These estimated weights highlight regions where initial errors are particularly sensitive. As a result, the analogs selected with weighted input follow the target trajectory closer than traditional analogs. Additionally, the convolutional neural network employed in our study exhibits robust improvements across various network sizes.

The application to ENSO forecasting shows significant improvements in perfect model skill at 6–18 months leads. The most significant improvements are observed in the central equatorial Pacific region and in predicting extreme events due to the large SST variability. Once optimized analogs are identified based on weighted distances, their subsequent time evolution can be analyzed in any fields available in the original climate simulation dataset. We demonstrate that improving equatorial Pacific SST forecasts results in improving precipitation forecasting beyond the target region.

We additionally show improvements in real-world applications across many initialization months and extreme events, although certain initialization months exhibit a reduction in forecast skill. This is likely attributed to the use of a single climate model for both training and analog selection. Future works should address this challenge by mitigating the effects of model biases, potentially through the incorporation of multiple climate models and leveraging transfer learning techniques.

The hybrid approach predicts weights linked to various known physical processes. Specifically, SST weights exhibit patterns similar to NPMm peaking in boreal spring and SPMm peaking in boreal winter. SSH weights are concentrated over the equatorial Pacific, likely capturing states linked to the recharge-discharge of warm water volume associated with ENSO oscillatory behavior. TAUX weights are large in regions where stochastic wind forcing typically occurs, with a peak in boreal summer. Furthermore, some weights are distributed over the Atlantic and Indian Ocean, indicating the influence of the tropical interbasin interactions. These weights are generated by the neural network method used, implying that it is straightforward to integrate superior deep learning algorithms for improved weight quantification.

There are many possible applications of this approach. It can be used for different climate phenomena across various regions, such as regional temperature and precipitation. This has been challenging with the unweighted model-analog because the selection of input variables and input regions must be made for each target, which could be subjective. The optimized model-analog approach addresses this issue by optimizing the focus (i.e., weights) in the input space using neural networks.

Another application is assessing the regional and variable contributions to forecasting skill. Broadly, two approaches can be considered: 1) training neural networks with restricted regions/variables, and 2) modifying (i.e., zeroing) predicted weights of certain

regions/variables. The first approach may yield results that are difficult to interpret due to correlations between used and unused features. On the other hand, the latter approach involves post-modification after model training and selects analogs without constraining a part of the input. This approach could provide interesting insights into quantifying the contribution of a specific feature by allowing error growth from that feature.

Acknowledgments.

This work was supported by the Famine Early Warning Systems Network and the NOAA Physical Sciences Laboratory. Jakob Schlör was supported by EXC number 2064/1 – Project number 390727645 and the International Max Planck Research School for Intelligent Systems (IMPRS-IS).

Data Availability Statement.

The CESM2-LE dataset is available from The National Center for Atmospheric Research (<https://doi.org/10.26024/kgmp-c556>). The ORAS5 dataset is available from the European Centre for Medium-Range Weather Forecasts (<https://doi.org/10.24381/cds.67e8eeb7>). The optimized model-analog codes are publicly available on GitHub (<https://github.com/kinyatoride/DLMA>).

APPENDIX

Appendix A Unweighted model-analog

This section presents the sensitivity of unweighted model-analog results to some parameters. Fig. A1a shows a skill comparison among different input regions and variables. The highest skill is achieved with SST and SSH over the tropics (30°S–30°N), as used in Lou et al. (2023). Expanding the input domain to the extratropics and including TAUX lead to a degradation in skill. Although the optimized model-analog approach assigns weights to the three variables over 50°S–50°N, we choose the one with SST and SSH over the tropics to avoid underestimating the skill of the unweighted approach.

Fig. A1b shows the sensitivity to analog member size. RMSE clearly worsens with a member size of fewer than 10. We select a member size of 30, which minimizes RMSE at lead times of 6–12 months.

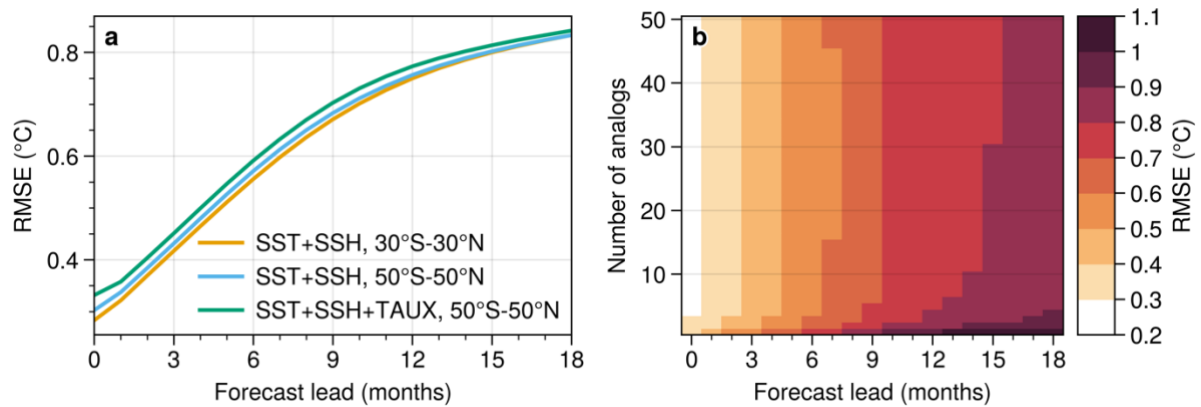


Fig. A1. (a) RMSE of equatorial Pacific SST as a function of forecast lead on the test dataset. Three unweighted model-analog approaches with different inputs are evaluated. (b) RMSE of equatorial Pacific SST as a function of forecast lead and analog member size.

Appendix B Lead time dependence

Fig. B1 shows a comparison of RMSE reduction using different forecast errors in the loss function. The model is trained with MSE at a specific lead time (3, 6, 9, or 12 months) in addition to using averaged MSE over 3, 6, 9, and 12 months leads. Note that the learning rate is fine-tuned independently. While the training results with a lead time of 3 months exhibit significantly different behavior, other results display more similarity. This tendency is also observed in the estimated weights, where the 3-month lead results focus more on the tropical Pacific (not shown). Among longer leads, the 6-month lead results yield the highest skill, especially for shorter leads. The results with the averaged MSE are slightly worse around 6-month lead but generally comparable to the 6-month lead results. Considering the potential dependency on the initial month for training results at specific lead times, we use the averaged MSE in this study.

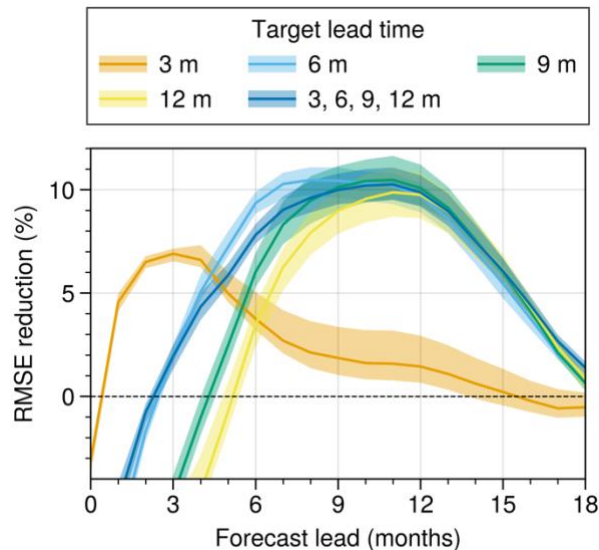


Fig. B1. RMSE reduction (%) of equatorial Pacific SST as a function of forecast lead for January initialization using the test dataset. The optimized model-analog is trained for various lead times. Shading shows the spread due to random initialization of network parameters.

REFERENCES

- Alexander, M. A., I. Bladé, M. Newman, J. R. Lanzante, N.-C. Lau, and J. D. Scott, 2002: The Atmospheric Bridge: The Influence of ENSO Teleconnections on Air–Sea Interaction over the Global Oceans. *Journal of Climate*, **15**, 2205–2231, [https://doi.org/10.1175/1520-0442\(2002\)015<2205:TABTIO>2.0.CO;2](https://doi.org/10.1175/1520-0442(2002)015<2205:TABTIO>2.0.CO;2).
- Amaya, D. J., 2019: The Pacific Meridional Mode and ENSO: a Review. *Curr Clim Change Rep*, **5**, 296–307, <https://doi.org/10.1007/s40641-019-00142-x>.
- Barsugli, J. J., and P. D. Sardeshmukh, 2002: Global Atmospheric Sensitivity to Tropical SST Anomalies throughout the Indo-Pacific Basin. *Journal of Climate*, **15**, 3427–3442, [https://doi.org/10.1175/1520-0442\(2002\)015<3427:GASTTS>2.0.CO;2](https://doi.org/10.1175/1520-0442(2002)015<3427:GASTTS>2.0.CO;2).
- Bellenger, H., E. Guilyardi, J. Leloup, M. Lengaigne, and J. Vialard, 2014: ENSO representation in climate models: from CMIP3 to CMIP5. *Clim Dyn*, **42**, 1999–2018, <https://doi.org/10.1007/s00382-013-1783-z>.
- Benjamini, Y., and Y. Hochberg, 1995: Controlling the False Discovery Rate: A Practical and Powerful Approach to Multiple Testing. *Journal of the Royal Statistical Society: Series B (Methodological)*, **57**, 289–300, <https://doi.org/10.1111/j.2517-6161.1995.tb02031.x>.
- Cachay, S. R., E. Erickson, A. F. C. Bucker, E. Pokropek, W. Potosnak, S. Bire, S. Osei, and B. Lütjens, 2021: The World as a Graph: Improving El Niño Forecasts with Graph Neural Networks. <https://doi.org/10.48550/arXiv.2104.05089>.

- Cai, W., and Coauthors, 2019: Pantropical climate interactions. *Science*, **363**, eaav4236, <https://doi.org/10.1126/science.aav4236>.
- Capotondi, A., and P. D. Sardeshmukh, 2015: Optimal precursors of different types of ENSO events. *Geophysical Research Letters*, **42**, 9952–9960, <https://doi.org/10.1002/2015GL066171>.
- , and L. Ricciardulli, 2021: The influence of pacific winds on ENSO diversity. *Sci Rep*, **11**, 18672, <https://doi.org/10.1038/s41598-021-97963-4>.
- , and Coauthors, 2015: Understanding ENSO Diversity. *Bulletin of the American Meteorological Society*, **96**, 921–938, <https://doi.org/10.1175/BAMS-D-13-00117.1>.
- , P. D. Sardeshmukh, and L. Ricciardulli, 2018: The Nature of the Stochastic Wind Forcing of ENSO. *Journal of Climate*, **31**, 8081–8099, <https://doi.org/10.1175/JCLI-D-17-0842.1>.
- Capotondi, A., C. Deser, A. S. Phillips, Y. Okumura, and S. M. Larson, 2020: ENSO and Pacific Decadal Variability in the Community Earth System Model Version 2. *Journal of Advances in Modeling Earth Systems*, **12**, e2019MS002022, <https://doi.org/10.1029/2019MS002022>.
- Chattopadhyay, A., E. Nabizadeh, and P. Hassanzadeh, 2020: Analog Forecasting of Extreme-Causing Weather Patterns Using Deep Learning. *Journal of Advances in Modeling Earth Systems*, **12**, e2019MS001958, <https://doi.org/10.1029/2019MS001958>.
- Chen, N., F. Gilani, and J. Harlim, 2021: A Bayesian Machine Learning Algorithm for Predicting ENSO Using Short Observational Time Series. *Geophysical Research Letters*, **48**, e2021GL093704, <https://doi.org/10.1029/2021GL093704>.
- Chiang, J. C. H., and D. J. Vimont, 2004: Analogous Pacific and Atlantic Meridional Modes of Tropical Atmosphere–Ocean Variability. *Journal of Climate*, **17**, 4143–4158, <https://doi.org/10.1175/JCLI4953.1>.
- Ding, H., M. Newman, M. A. Alexander, and A. T. Wittenberg, 2018: Skillful Climate Forecasts of the Tropical Indo-Pacific Ocean Using Model-Analogs. *Journal of Climate*, **31**, 5437–5459, <https://doi.org/10.1175/JCLI-D-17-0661.1>.
- , ———, ———, and ———, 2019: Diagnosing Secular Variations in Retrospective ENSO Seasonal Forecast Skill Using CMIP5 Model-Analogs. *Geophysical Research Letters*, **46**, 1721–1730, <https://doi.org/10.1029/2018GL080598>.
- Errico, R. M., 1997: What Is an Adjoint Model? *Bulletin of the American Meteorological Society*, **78**, 2577–2592, [https://doi.org/10.1175/1520-0477\(1997\)078<2577:WIAAM>2.0.CO;2](https://doi.org/10.1175/1520-0477(1997)078<2577:WIAAM>2.0.CO;2).
- Ham, Y.-G., J.-H. Kim, and J.-J. Luo, 2019: Deep learning for multi-year ENSO forecasts. *Nature*, **573**, 568–572, <https://doi.org/10.1038/s41586-019-1559-7>.

- , ——, E.-S. Kim, and K.-W. On, 2021: Unified deep learning model for El Niño/Southern Oscillation forecasts by incorporating seasonality in climate data. *Science Bulletin*, **66**, 1358–1366, <https://doi.org/10.1016/j.scib.2021.03.009>.
- Hamill, T. M., 2001: Interpretation of Rank Histograms for Verifying Ensemble Forecasts. *Monthly Weather Review*, **129**, 550–560, [https://doi.org/10.1175/1520-0493\(2001\)129<0550:IORHFV>2.0.CO;2](https://doi.org/10.1175/1520-0493(2001)129<0550:IORHFV>2.0.CO;2).
- He, K., X. Zhang, S. Ren, and J. Sun, 2015: Deep Residual Learning for Image Recognition. <https://doi.org/10.48550/arXiv.1512.03385>.
- Hersbach, H., 2000: Decomposition of the Continuous Ranked Probability Score for Ensemble Prediction Systems. *Weather and Forecasting*, **15**, 559–570, [https://doi.org/10.1175/1520-0434\(2000\)015<0559:DOTCRP>2.0.CO;2](https://doi.org/10.1175/1520-0434(2000)015<0559:DOTCRP>2.0.CO;2).
- Hoell, A., and C. Funk, 2013: The ENSO-Related West Pacific Sea Surface Temperature Gradient. *Journal of Climate*, **26**, 9545–9562, <https://doi.org/10.1175/JCLI-D-12-00344.1>.
- Jin, F.-F., 1997: An Equatorial Ocean Recharge Paradigm for ENSO. Part I: Conceptual Model. *Journal of the Atmospheric Sciences*, **54**, 811–829, [https://doi.org/10.1175/1520-0469\(1997\)054<0811:AEORPF>2.0.CO;2](https://doi.org/10.1175/1520-0469(1997)054<0811:AEORPF>2.0.CO;2).
- Kingma, D. P., and J. Ba, 2017: Adam: A Method for Stochastic Optimization. <https://doi.org/10.48550/arXiv.1412.6980>.
- Larson, S. M., and B. P. Kirtman, 2014: The Pacific Meridional Mode as an ENSO Precursor and Predictor in the North American Multimodel Ensemble. *Journal of Climate*, **27**, 7018–7032, <https://doi.org/10.1175/JCLI-D-14-00055.1>.
- Lorenz, E. N., 1963: Deterministic Nonperiodic Flow. *Journal of the Atmospheric Sciences*, **20**, 130–141, [https://doi.org/10.1175/1520-0469\(1963\)020<0130:DNF>2.0.CO;2](https://doi.org/10.1175/1520-0469(1963)020<0130:DNF>2.0.CO;2).
- , 1969a: Atmospheric Predictability as Revealed by Naturally Occurring Analogues. *Journal of the Atmospheric Sciences*, **26**, 636–646, [https://doi.org/10.1175/1520-0469\(1969\)26<636:APARBN>2.0.CO;2](https://doi.org/10.1175/1520-0469(1969)26<636:APARBN>2.0.CO;2).
- , 1969b: The predictability of a flow which possesses many scales of motion. *Tellus*, **21**, 289–307, <https://doi.org/10.1111/j.2153-3490.1969.tb00444.x>.
- Lou, J., M. Newman, and A. Hoell, 2023: Multi-decadal variation of ENSO forecast skill since the late 1800s. *npj Clim Atmos Sci*, **6**, 1–14, <https://doi.org/10.1038/s41612-023-00417-z>.
- Mamalakis, A., E. A. Barnes, and I. Ebert-Uphoff, 2022: Investigating the Fidelity of Explainable Artificial Intelligence Methods for Applications of Convolutional Neural Networks in Geoscience. *Artificial Intelligence for the Earth Systems*, **1**, <https://doi.org/10.1175/AIES-D-22-0012.1>.
- McPhaden, M. J., 2003: Tropical Pacific Ocean heat content variations and ENSO persistence barriers. *Geophysical Research Letters*, **30**, <https://doi.org/10.1029/2003GL016872>.

- Meinen, C. S., and M. J. McPhaden, 2000: Observations of Warm Water Volume Changes in the Equatorial Pacific and Their Relationship to El Niño and La Niña. *Journal of Climate*, **13**, 3551–3559, [https://doi.org/10.1175/1520-0442\(2000\)013<3551:OOWWVC>2.0.CO;2](https://doi.org/10.1175/1520-0442(2000)013<3551:OOWWVC>2.0.CO;2).
- Menkes, C. E., M. Lengaigne, J. Vialard, M. Puy, P. Marchesiello, S. Cravatte, and G. Cambon, 2014: About the role of Westerly Wind Events in the possible development of an El Niño in 2014. *Geophysical Research Letters*, **41**, 6476–6483, <https://doi.org/10.1002/2014GL061186>.
- Mulholland, D. P., P. Laloyaux, K. Haines, and M. A. Balmaseda, 2015: Origin and Impact of Initialization Shocks in Coupled Atmosphere–Ocean Forecasts. *Monthly Weather Review*, **143**, 4631–4644, <https://doi.org/10.1175/MWR-D-15-0076.1>.
- Newman, M., and P. D. Sardeshmukh, 2017: Are we near the predictability limit of tropical Indo-Pacific sea surface temperatures? *Geophysical Research Letters*, **44**, 8520–8529, <https://doi.org/10.1002/2017GL074088>.
- Oktaý, O., and Coauthors, 2018: Attention U-Net: Learning Where to Look for the Pancreas. <https://doi.org/10.48550/arXiv.1804.03999>.
- Penland, C., and P. D. Sardeshmukh, 1995: The Optimal Growth of Tropical Sea Surface Temperature Anomalies. *Journal of Climate*, **8**, 1999–2024, [https://doi.org/10.1175/1520-0442\(1995\)008<1999:TOGOTS>2.0.CO;2](https://doi.org/10.1175/1520-0442(1995)008<1999:TOGOTS>2.0.CO;2).
- Petersik, P. J., and H. A. Dijkstra, 2020: Probabilistic Forecasting of El Niño Using Neural Network Models. *Geophysical Research Letters*, **47**, e2019GL086423, <https://doi.org/10.1029/2019GL086423>.
- Rader, J. K., and E. A. Barnes, 2023: Optimizing Seasonal-To-Decadal Analog Forecasts With a Learned Spatially-Weighted Mask. *Geophysical Research Letters*, **50**, e2023GL104983, <https://doi.org/10.1029/2023GL104983>.
- Risbey, J. S., and Coauthors, 2021: Standard assessments of climate forecast skill can be misleading. *Nat Commun*, **12**, 4346, <https://doi.org/10.1038/s41467-021-23771-z>.
- Rodgers, K. B., and Coauthors, 2021: Ubiquity of human-induced changes in climate variability. *Earth System Dynamics*, **12**, 1393–1411, <https://doi.org/10.5194/esd-12-1393-2021>.
- Ronneberger, O., P. Fischer, and T. Brox, 2015: U-Net: Convolutional Networks for Biomedical Image Segmentation. *Medical Image Computing and Computer-Assisted Intervention – MICCAI 2015*, N. Navab, J. Hornegger, W.M. Wells, and A.F. Frangi, Eds., *Lecture Notes in Computer Science*, Cham, Springer International Publishing, 234–241.
- Roulston, M. S., and J. D. Neelin, 2000: The response of an ENSO Model to climate noise, weather noise and intraseasonal forcing. *Geophysical Research Letters*, **27**, 3723–3726, <https://doi.org/10.1029/2000GL011941>.

- Shin, N.-Y., Y.-G. Ham, J.-H. Kim, M. Cho, and J.-S. Kug, 2022: Application of Deep Learning to Understanding ENSO Dynamics. *Artificial Intelligence for the Earth Systems*, **1**, <https://doi.org/10.1175/AIES-D-21-0011.1>.
- Shin, S.-I., P. D. Sardeshmukh, M. Newman, C. Penland, and M. A. Alexander, 2021: Impact of Annual Cycle on ENSO Variability and Predictability. *Journal of Climate*, **34**, 171–193, <https://doi.org/10.1175/JCLI-D-20-0291.1>.
- Taschetto, A. S., C. C. Ummerhofer, M. F. Stuecker, D. Dommenges, K. Ashok, R. R. Rodrigues, and S.-W. Yeh, 2020: ENSO Atmospheric Teleconnections. *El Niño Southern Oscillation in a Changing Climate*, American Geophysical Union (AGU), 309–335.
- Van den Dool, H. M., 1989: A New Look at Weather Forecasting through Analogues. *Monthly Weather Review*, **117**, 2230–2247, [https://doi.org/10.1175/1520-0493\(1989\)117<2230:ANLAWF>2.0.CO;2](https://doi.org/10.1175/1520-0493(1989)117<2230:ANLAWF>2.0.CO;2).
- Vimont, D. J., M. A. Alexander, and M. Newman, 2014: Optimal growth of Central and East Pacific ENSO events. *Geophysical Research Letters*, **41**, 4027–4034, <https://doi.org/10.1002/2014GL059997>.
- Wang, C., 2019: Three-ocean interactions and climate variability: a review and perspective. *Clim Dyn*, **53**, 5119–5136, <https://doi.org/10.1007/s00382-019-04930-x>.
- Wilks, D. S., 2016: “The Stippling Shows Statistically Significant Grid Points”: How Research Results are Routinely Overstated and Overinterpreted, and What to Do about It. *Bulletin of the American Meteorological Society*, **97**, 2263–2273, <https://doi.org/10.1175/BAMS-D-15-00267.1>.
- You, Y., and J. C. Furtado, 2018: The South Pacific Meridional Mode and Its Role in Tropical Pacific Climate Variability. *Journal of Climate*, **31**, 10141–10163, <https://doi.org/10.1175/JCLI-D-17-0860.1>.
- Zhang, H., A. Clement, and P. D. Nezio, 2014: The South Pacific Meridional Mode: A Mechanism for ENSO-like Variability. *Journal of Climate*, **27**, 769–783, <https://doi.org/10.1175/JCLI-D-13-00082.1>.
- Zhou, L., and R.-H. Zhang, 2023: A self-attention–based neural network for three-dimensional multivariate modeling and its skillful ENSO predictions. *Science Advances*, **9**, eadf2827, <https://doi.org/10.1126/sciadv.adf2827>.
- Zuo, H., M. A. Balmaseda, S. Tietsche, K. Mogensen, and M. Mayer, 2019: The ECMWF operational ensemble reanalysis–analysis system for ocean and sea ice: a description of the system and assessment. *Ocean Science*, **15**, 779–808, <https://doi.org/10.5194/os-15-779-2019>.